Use of along-track magnetic field differences in lithospheric field modelling

S. Kotsiaros, C. C. Finlay and N. Olsen

DTU Space, Technical University of Denmark, Elektrovej 328, 2800 Kgs. Lyngby, Denmark. E-mail: skotsiaros@space.dtu.dk

SUMMARY

We demonstrate that first differences of polar orbiting satellite magnetic data in the along-track direction can be used to obtain high resolution models of the lithospheric field. Along-track differences approximate the north–south magnetic field gradients for non-polar latitudes. In a test case, using 2 yr of low altitude data from the CHAMP satellite, we show that use of along-track differences of vector field data results in an enhanced recovery of the small scale lithospheric field, compared to the use of the vector field data themselves. We show that the along-track technique performs especially well in the estimation of near zonal spherical harmonic coefficients. Moreover, lithospheric field models determined using along-track differences are found to be less sensitive to the presence of unmodelled external field contributions and problems associated with the polar gap are ameliorated. Experiments in modelling the Earth's lithospheric magnetic field with along-track differences are presented here as a proof of concept. We anticipate that use of such along-track differences in combination with east–west field differences, as are now provided by the Swarm satellite constellation, will be important in building the next generation of lithospheric field models.

Key words: Inverse theory; Magnetic anomalies: modelling and interpretation; Satellite magnetics.

1 INTRODUCTION

Satellites in low-Earth orbit provide the most effective means of determining on a global scale the magnetic field arising from the magnetization of the lithosphere. In particular, the CHAMP satellite, *cf.* Reigber *et al.* (2005), provided high-precision magnetic field observations, with a wide time–space coverage, at low altitude and during solar minimum, which has led to detailed and precise magnetic field models of the Earth's lithosphere. Such models are the magnetic field (MF) model series, for example MF7[1] (Maus *et al.* 2008), and the comprehensive model (CM) series, for example CM5 (Sabaka *et al.* 2014), the CHAMP, Ørsted and SAC-C model series of Earth's magnetic field (CHAOS), for example CHAOS-4 (Olsen *et al.* 2014), and the GFZ reference internal magnetic model (GRIMM) series (e.g. Lesur *et al.* 2013). Detailed discussion of recent progress in lithospheric field modelling using satellites can also be found in the reviews by Thébault *et al.* (2010) and Olsen & Stolle (2012).

Data from the Swarm satellites (Friis-Christensen *et al.* 2006), launched in 2013 November, will in the upcoming years provide an opportunity to study on a global scale lithospheric field features with increased resolution compared to the present CHAMP-based models. This is possible thanks to the pair of Swarm satellites that are flying side-by-side, providing estimates of the east–west gradient of the magnetic field. There have been several studies investigating the use of magnetic field gradient data within well understood synthetic simulations. Thébault *et al.* (2013) have documented the advantages of using east–west field gradients in a regional modelling scheme in order to better detect small scale lithospheric field signatures. Sabaka *et al.* (2013) show how, within their comprehensive modelling framework co-estimating a large number of sources, sums and differences of satellite data can be used to aid both small scale lithospheric field retrieval and source separation. On the other hand, studying the case of ideal gradients, Kotsiaros & Olsen (2014) have emphasized that while east–west gradients provide information on the sectoral and tesseral spherical harmonic components, north–south gradients provide complementary information on the zonal and near-zonal modelling terms.

Here, we present a study with real data (CHAMP measurements obtained during the final 2 yr of that mission) and propose a way to approximate north–south gradients by forming the first differences of the vector data along each track of the satellite orbit. We emphasize that due to the Earth's rotation, and because the north–south gradients are not approximated instantaneously, along-track differences contain a mixture of north–south and east–west gradient signals. Along-track differences of satellite magnetic data have previously been used in studies of planetary magnetism in

[1] www.geomag.us/models/MF7/MF7.html.

order to enhance the resolution of the lithospheric field, for example Connerney *et al.* (2005) has derived maps of the Martian magnetic field by binning and processing along-track differences. On the other hand, we are not aware of any study where real along-track satellite magnetic data have been used to derive a full potential magnetic field model in spherical harmonic form. Here, we use along-track differences from CHAMP to derive models of the Earth's lithospheric magnetic field and compare these with models estimated using the standard approach involving vector field data themselves. In Sections 2 and 3, we present our selection and processing of the CHAMP data, and the adopted field modelling scheme, respectively. In Section 4, we present results including investigations of various spacings (samplings) of along-track differences, comparisons between similar models derived with along-track and standard vector field data, as well as detailed comparisons with the MF7 and CM5 models derived using alternative modelling methods. CM5 is a very recent field model derived from CHAMP, Ørsted and SAC-C satellite and observatory hourly means data from 2000 August to 2013 January. Compared to its predecessor (i.e. CM4), a new treatment for attitude error in satellite vector measurements was deployed and a 3-D conductivity model considered for induction due to solar-quiet current system is included. More importantly in the present context, CM5 uses CHAMP along-track differences for the estimation of the high degree ($n \geq 60$) lithospheric field. For more details on CM5 see Sabaka *et al.* (2014). The relative importance of unmodelled external field fluctuations for models derived using along-track and standard vector data is also studied and experiments related to the polar gap problem are reported in Section 4. Finally, in Section 5, we conclude with a summary of our findings and remark on possible future exploitations of along-track differences, focusing our attention on possibilities regarding the Swarm mission.

2 DATA SELECTION

We adopt similar data selection criteria to those employed for determining the CHAOS model series, for example Olsen *et al.* (2006, 2014). In particular, we select CHAMP vector data only between 2008 September and 2010 September, a period characterized by solar minimum conditions. This results in a relatively large amount of quiet-time data and minimizes the contamination of the lithospheric field determination by plasma irregularities in the ionosphere and magnetosphere, notable at times of higher solar activity (Lühr *et al.* 2003). Furthermore, the chosen time interval is towards the end of the CHAMP mission when the satellite altitude was at its lowest, that is below 300 km, thus providing data that are more sensitive to the small scale lithospheric field. In order to to reduce contributions from ionospheric currents, only data from dark regions, when the sun is $10°$ below horizon, were used. All data are selected according to quiet geomagnetic conditions. First, it was required that $|\frac{dD_{st}}{dt}| \leq 2 \frac{nT}{hr}$ at all latitudes. At quasi-dipole (QD) latitudes (Richmond 1995) equatorwards of $\pm55°$, $K_p \leq 2o$ has to be fulfilled, whereas polewards of $\pm55°$ it is required that the merging magnetic field, E_m, at the magnetopause is less than $0.8 \frac{mV}{m}$. To avoid the disturbing effect of the field-aligned currents, three component vector field data have been taken only at QD latitudes equatorwards of $\pm55°$. At higher latitudes, we used solely the radial field component, B_r, which led to better field models than with the more common approach of using scalar field intensity data. However, using the along-track differences, tests with scalar field intensity data at high latitudes resulted in almost identical field models.

In an effort to keep things as simple as possible and to focus on modelling the lithospheric field, CHAOS-4 model (Olsen *et al.* 2014) predictions for both the core field $\mathbf{B}_{core}$ (up to spherical harmonic degree $N = 15$) and the large-scale magnetospheric field $\mathbf{B}_{mag}$ were subtracted from the CHAMP observations, $\mathbf{B}_{obs}$, prior to modelling.

$$\tilde{\mathbf{B}} = \mathbf{B}_{obs} - \mathbf{B}_{core} - \mathbf{B}_{mag} \tag{1}$$

$$= \mathbf{B}_{lith} + \epsilon, \tag{2}$$

where $\mathbf{B}_{lith}$ is the true lithospheric signal and ϵ the remaining contamination errors, primarily due to unmodelled field contributions for example due to ionospheric currents, field-aligned currents, and unmodelled induced currents (e.g. Kunagu *et al.* 2013).

3 MODEL PARAMETRIZATION AND ESTIMATION

We adopt a potential field model, assuming that there are no electrical currents in the data sampling region. Under this assumption, we can write the modelled vector magnetic field $\mathbf{B}_{mod}$, at any location within this region, as the gradient of a scalar magnetic potential V. For example in the local north, east, centre (NEC) coordinate system,

$$\mathbf{B}_{mod} = \begin{bmatrix} B_{North} \\ B_{East} \\ B_{Center} \end{bmatrix} = \begin{bmatrix} -B_\theta \\ +B_\phi \\ -B_r \end{bmatrix} = -\nabla V, \tag{3}$$

The potential V satisfies Laplace's equation so it can be expressed by a spherical harmonic expansion. We consider only internal sources, in which case the appropriate expression for V is:

$$V = a \sum_{n=1}^{N} \sum_{m=0}^{n} \left(g_n^m \cos m\phi + h_n^m \sin m\phi\right) \left(\frac{a}{r}\right)^{n+1} P_n^m(\cos\theta), \tag{4}$$

where $a = 6371.2$ km is the spherical reference radius of Earth's surface, (r, θ, ϕ) are geographic coordinates, P_n^m are the Schmidt semi-normalized associated Legendre functions, $\{g_n^m, h_n^m\}$ are the Gauss coefficients describing internal sources and N is the maximum degree and order of the expansion, taken here to be $N = 120$.

To estimate the model parameters $\mathbf{m} = \{g_n^m, h_n^m\}$ from the satellite magnetic field data we adopt a least-squares approach. Collecting the data $\tilde{\mathbf{B}}$ from all observation locations into a vector $\tilde{\mathbf{d}}$ and the associated model predictions $\mathbf{B}_{mod}$ into a vector $\mathbf{d}_{mod}$, this involves minimizing the sum of the squares of the residual vector $\mathbf{e} = \tilde{\mathbf{d}} - \mathbf{d}_{mod}$.

The residuals, $\mathbf{e}$, are however not Gaussian distributed because our model is incomplete (i.e. there are remaining unmodelled fields). In this scenario, the standard least-squares estimate does not provide a reliable model estimate (Walker & Jackson 2000). To better handle the non-Gaussian residuals, we therefore follow an iteratively reweighted least-squares approach (*cf.* Huber 1964; Constable 1988). Our implementation is similar to that described by Olsen (2002) and has previously been used in the derivation of the CHAOS series of field models (Olsen *et al.* 2006, 2014). At each iteration, a data weight matrix, $\underline{\mathbf{W}}$, is assigned which reflects a Huber distribution with a Gaussian core and Laplacian tails (the threshold parameter for this transition is chosen to be 1.5) and we then minimize the cost function

$$\left(\tilde{\mathbf{d}} - \mathbf{d}_{mod}\right)^T \underline{\mathbf{W}} \left(\tilde{\mathbf{d}} - \mathbf{d}_{mod}\right), \tag{5}$$

where

$$\mathbf{d}_{\mathrm{mod}} = \underline{\underline{\mathbf{G}}}\mathbf{m}, \tag{6}$$

where $\underline{\underline{\mathbf{G}}}$ is the design matrix relating the model parameters $\mathbf{m}$ to the magnetic field predictions $\mathbf{d}_{\mathrm{mod}}$. For our experiments, a model derived from vector data has been computed using (6). At the ith iteration, the model parameters are determined as

$$\mathbf{m}_i = [\underline{\underline{\mathbf{G}}}^T \underline{\underline{\mathbf{W}}}_i \, \underline{\underline{\mathbf{G}}}]^{-1}[\underline{\underline{\mathbf{G}}}^T \underline{\underline{\mathbf{W}}}_i] \tilde{\mathbf{d}}, \tag{7}$$

and the resulting residuals $\mathbf{e}$ are used to update the data weight matrix $\underline{\underline{\mathbf{W}}}_{i+1}$. The number of iterations is based on the convergence of the estimated model parameters. In our case, convergence is achieved after four iterations.

When considering along-track differences rather than standard vector field data we instead minimize the square of the residuals $\Delta\mathbf{e} = \Delta\tilde{\mathbf{d}} - \Delta\mathbf{d}_{\mathrm{mod}}$ between along-track differences of data $\Delta\tilde{\mathbf{d}} = \tilde{\mathbf{d}}(\mathbf{r}_2, t_2) - \tilde{\mathbf{d}}(\mathbf{r}_1, t_1)$ and the associated along-track differences of model predictions $\Delta\mathbf{d}_{\mathrm{mod}} = \mathbf{d}_{\mathrm{mod}}(\mathbf{r}_2, t_2) - \mathbf{d}_{\mathrm{mod}}(\mathbf{r}_1, t_1)$. Here, $(\mathbf{r}_1, t_1)$ is the location and time of the first datum contributing to the along-track difference and $(\mathbf{r}_2, t_2)$ is the location and time of the second datum. Note that $t_2 > t_1$ since it refers to the next sampled location along the satellite orbit track. In this situation, the cost function minimized for the along-track difference data becomes

$$\left(\Delta\tilde{\mathbf{d}} - \Delta\mathbf{d}_{\mathrm{mod}}\right)^T \underline{\underline{\mathbf{W}}} \left(\Delta\tilde{\mathbf{d}} - \Delta\mathbf{d}_{\mathrm{mod}}\right), \tag{8}$$

where now

$$\Delta\mathbf{d}_{\mathrm{mod}} = \Delta\underline{\underline{\mathbf{G}}}\mathbf{m}, \tag{9}$$

and $\Delta\underline{\underline{\mathbf{G}}} = \underline{\underline{\mathbf{G}}}(\mathbf{r}_2, t_2) - \underline{\underline{\mathbf{G}}}(\mathbf{r}_1, t_1)$. Similarly to (7), at the ith iteration, the model parameters are determined from along-track difference data as

$$\mathbf{m}_i = [\Delta\underline{\underline{\mathbf{G}}}^T \underline{\underline{\mathbf{W}}}_i \, \Delta\underline{\underline{\mathbf{G}}}]^{-1}[\Delta\underline{\underline{\mathbf{G}}}^T \underline{\underline{\mathbf{W}}}_i]\Delta\tilde{\mathbf{d}}. \tag{10}$$

Neither filtering of the data nor regularization is applied during the model estimation procedure, in contrast to other recent models of the high degree lithospheric field (Maus *et al.* 2008; Lesur *et al.* 2013; Olsen *et al.* 2014). This helps highlight the differences between models constructed using only vector field data and models constructed using along-track differences of vector field data. However, we expect to see the impact of noise mapped into our models at very high degree.

4 RESULTS AND DISCUSSION

If one is to use along-track difference data, a first important question is what is the optimal choice of sampling rate for computing the differences. Distinctions between sampling rates can be identified even prior to field modelling with along-track difference data. For example, in the left-hand panel of Fig. 1 we present as a function of QD latitude the standard deviation of residuals (i.e. CHAMP observations minus CHAOS-4 model predictions for the core, lithospheric and magnetospheric field contributions) of the along-track differences of the radial field data divided by the along-track distance, that is $\Delta B_r/\Delta s$. Here, $\Delta B_r = B_r(t_2) - B_r(t_1)$ with $t_2 > t_1$, and Δs is the along-track spherical distance which CHAMP spans in the time $\Delta t = t_2 - t_1$, and this quantity approximates the north–south gradient for non-polar latitudes. The standard deviation is calculated using all (2 yr) data from the selected CHAMP data set. Subsequently, data are picked taking every k-th point, where $k = 15$, 30, 45 or 60. Results are presented for four different along-track samplings, Δt; $\Delta t_1 = 15$ s corresponds to a spacing of approximately 116 km at the Earth's surface, whereas $\Delta t_2 = 30$ s corresponds to 232 km, $\Delta t_3 = 45$ s to 347 km and $\Delta t_4 = 60$ s to 463 km. For QD latitudes polewards of $\pm 55°$, sampling $\Delta t_3 = 45$ s presents the lowest standard deviation. On the other hand, for mid and low QD latitudes below ± 55 the standard deviation of sampling $\Delta t_4 = 60$ s is slightly lower than that of $\Delta t_3 = 45$ s. In order to examine the noise levels of along-track difference data in comparison to vector data, the standard deviation of residuals of along-track differences of the radial field data ΔB_r (with $\Delta t_2 = 30$ s) and the standard deviation of residuals of radial field data B_r are plotted in the right-hand panel of Fig. 1. Assuming that the noise was randomly distributed, one would expect higher standard deviation by a factor of $\sqrt{2}$ in the along-track differences than in the vector data. However, it can be seen that the standard deviation of along-track differences is considerably reduced at almost all latitudes compared to the standard deviation of vector data. This is an encouraging result because it indicates that along-track difference data may be superior to standard vector data and may have advantages for lithospheric field modelling. An interesting point made by a reviewer is that the standard deviations in the northern (QD latitude between 60° and 90°) and southern (QD latitude between $-60°$ and $-90°$) polar regions are not equal. We do not know the reason for this asymmetry, which could for example be due to differences in ionospheric conditions (e.g. the electrical conductivity, flowing ionospheric currents, etc.) as well as the data distribution in the two polar regions not being identical.
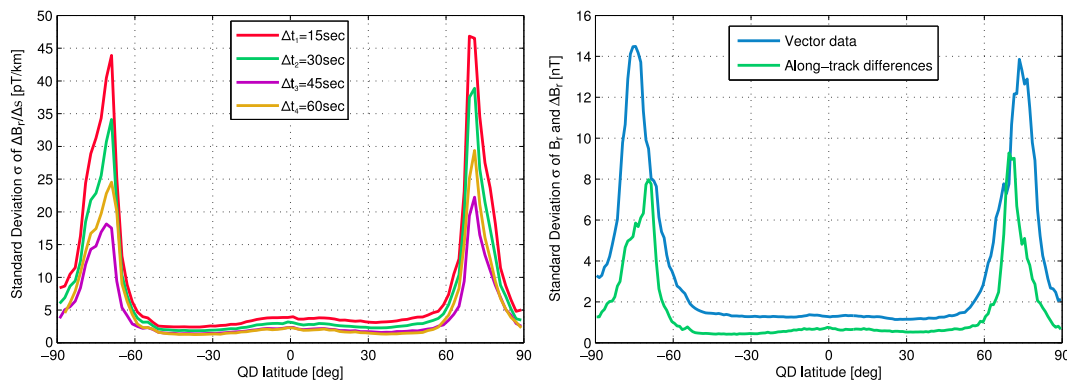
Figure 1. Left-hand panel: comparison of the standard deviation of along-track gradient $\frac{\Delta B_r}{\Delta s}$ residuals (CHAMP data minus CHAOS-4 model predictions) for four different sampling rates, $\Delta t_1 = 15$ s, $\Delta t_2 = 30$ s, $\Delta t_3 = 45$ s and $\Delta t_4 = 60$ s. Right-hand panel: comparison of standard deviation of residuals of along-track differences of radial field data ΔB_r (green line) and of residuals of radial field data B_r (blue line).
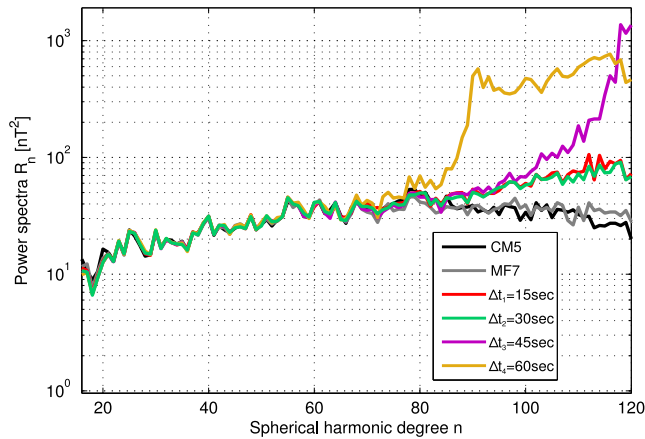
Figure 2. Comparison of Mauersberger–Lowes power spectra of lithospheric field models derived using four different along-track samplings, $\Delta t_1 = 15$ s, $\Delta t_2 = 30$ s, $\Delta t_3 = 45$ s and $\Delta t_4 = 60$ s.

Such considerations of the amplitude of the noise inherent in the along-track differences derived using different sampling rate are however not the whole story. When building a lithospheric field model, one must also choose a sampling rate high enough to adequately constrain the high degrees of the field model. Choosing a lower sampling rate, with longer spacings between the samples, may therefore not be advantageous, even if the noise level is reduced. To investigate the combined influence of these two effects we next derived four different lithospheric field models using CHAMP along-track differences with the four different samplings introduced above. The Mauersberger–Lowes power spectrum (Lowes 1974) is then used as a tool to identify the sampling that produces the best field model.

Fig. 2 compares the power spectra of lithospheric field models derived using samplings of $\Delta t_1 = 15$ s (red line) which results in 1 014 139 data points, $\Delta t_2 = 30$ s (green line) which results in 507 070 data points, $\Delta t_3 = 45$ s (magneta line) which results in 338 047 data points and $\Delta t_4 = 60$ s (yellow line) which

results in 253 535 data points for the interval studies. The spectra of CM5 (black line) and and MF7 (grey line) also shown for reference.

A first noteworthy result is that we succeeded in deriving stable lithospheric field models using the along-track difference data. The models derived using all investigated sampling rates show power spectra matching MF7 and CM5 relatively well up to approximately degree $n = 75$. The best agreement with CM5 and MF7 and a relatively consistent power spectrum above degree $n = 80$ is achieved using $\Delta t_2 = 30$ s. We henceforth adopt this as our preferred sampling rate. Note that data filtering has not been applied for deriving our lithospheric field models and the models have not been regularized even at high degree. In contrast, filtering and line levelling have been applied during the derivation of MF7 above degree $n = 77$ and 100, respectively (Maus *et al.* 2008), whereas CM5 is regularized above degree $n = 85$. This may partly account for why our preferred along-track model shows a positive slope above degree 85 while MF7 and CM5 possess a descending slope at high degree.

The divergence of the power spectrum above degree $n = 86$ for Δt_4 and above degree $n = 111$ for Δt_3 is likely due to the sampling rate becoming too low to properly constrain the spherical harmonic model. According to Backus *et al.* (1996), the shortest spatial wavelength at the Earth's surface captured by a spherical harmonic of degree n is 40 000 km/($n + 1/2$). For $n = 86$ this is approximately 462 km, very similar to the along-track spacing of Δt_4 (463 km). For higher $n > 86$ the sampling of Δt_4 is therefore insufficient. In contrast, the spacing of along-track differences for Δt_3, is sufficient up to spherical harmonic degree approximately $n = 111$, where the smallest represented wavelength is approximately 355 km. The maximum theoretical resolution for $\Delta t_2 = 30$ s on the other hand is $n = 172$, well above the truncation level chosen here. Fig. 3 presents maps of the radial magnetic field at the Earth's surface determined using standard vector field data (left-hand panel) and along-track difference data (right-hand panel), based on the same data set (with 30 s sampling rate) and the same model parametrization. Hereafter, we refer to the model derived from vector data as the 'vector model' and the model derived from along-track differences as the 'along-track' model. These maps were produced using degrees $n = 16$–90
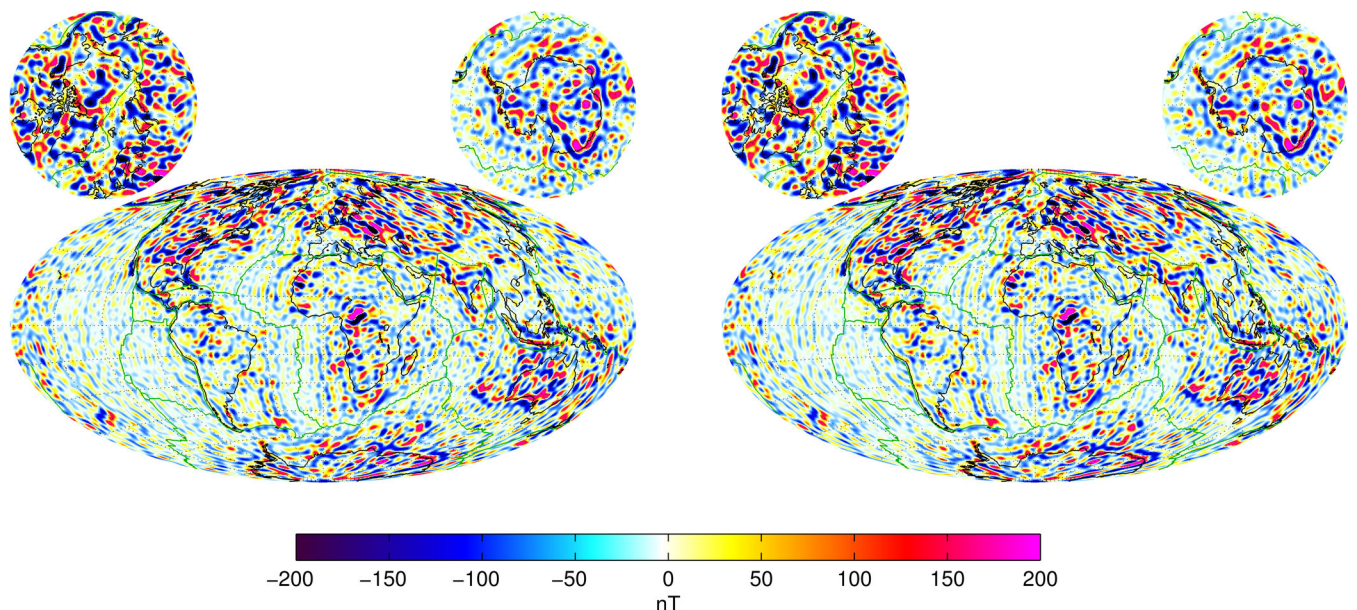

Figure 3. Maps of radial lithospheric magnetic field calculated at the Earth's surface from coefficients of degrees $n = 16$–90 taken from the field model derived from vector data (left-hand panel) and from the model derived from along-track differences of vector field data with our preferred sampling of $\Delta t_2 = 30$ s (right-hand panel).
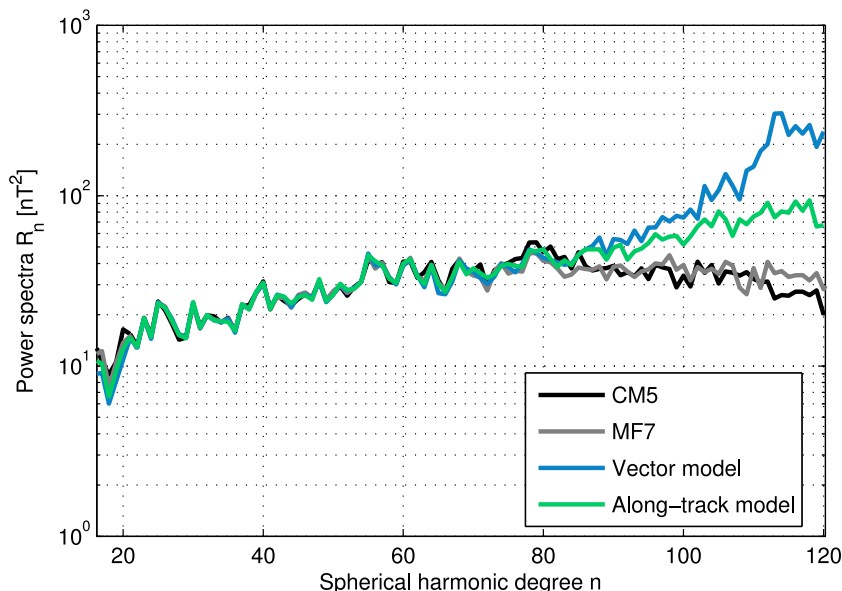
Figure 4. Comparison of Mauersberger–Lowes power spectra for the vector model (blue) and the along-track model (green) compared with CM5 (black) and MF7 (grey).

of the respective lithospheric field models. The lithospheric field resulting from the along-track model is reasonable and shows similar structures to the vector model. The along-track model may even be superior to the vector model with respect to the retrieved lithospheric field features. For example, fewer spurious features are observed in the south of Australia where the lithospheric field is weak. In addition, features in the polar regions and in the northwest of south America are more clearly defined in the along-track than the vector model.

In Fig. 4, we present a comparison of power spectra of the vector model (blue line) and of the along-track model (green line). The power spectra of CM5 (black), *cf.* Sabaka *et al.* (2014) and MF7 (grey), *cf.* Maus *et al.* (2008) are again included for reference. It is evident that the spectrum of the along-track model is closer to that of CM5 and MF7 than the vector model, especially above degree $n = 85$, illustrating the advantage of using along-track data. The power spectrum of the vector model on the other hand increases more rapidly, especially above degree 100. We conclude that using along-track data results in models that are less influenced by noise at high degree.

Moving beyond a comparison in terms of the power spectra, in Fig. 5 we analyse the relative phase of the vector and along-track models compared to MF7 (left-hand panel) and CM5 (right-hand panel), using the degree correlation ρ_n, as defined by Langel & Hinze (1998). For reference, the degree correlation of CM5 with MF7 is also plotted. We find that the along-track model generally has a superior correlation with both MF7 and CM5 than the vector model. In particular, the correlation of the along-track model with MF7 is noticeably better than with CM5 at high degrees $n > 90$. Taken together, the power spectra and the degree correlation seem to demonstrate the superiority of the along-track model over the vector model.

Further insight is gained by considering the so-called sensitivity matrices (*cf.* Olsen *et al.* 2006) presented in Fig. 6. These show the relative difference between each coefficient of the vector model (left-hand panels) or the along-track model (right-hand panels) and either MF7 (top panels) or CM5 (bottom panels). The along-track model is again found to be in better agreement with both MF7 and CM5, especially for degrees $n > 80$. In particular, the sensitivity matrices demonstrate how the along-track model better
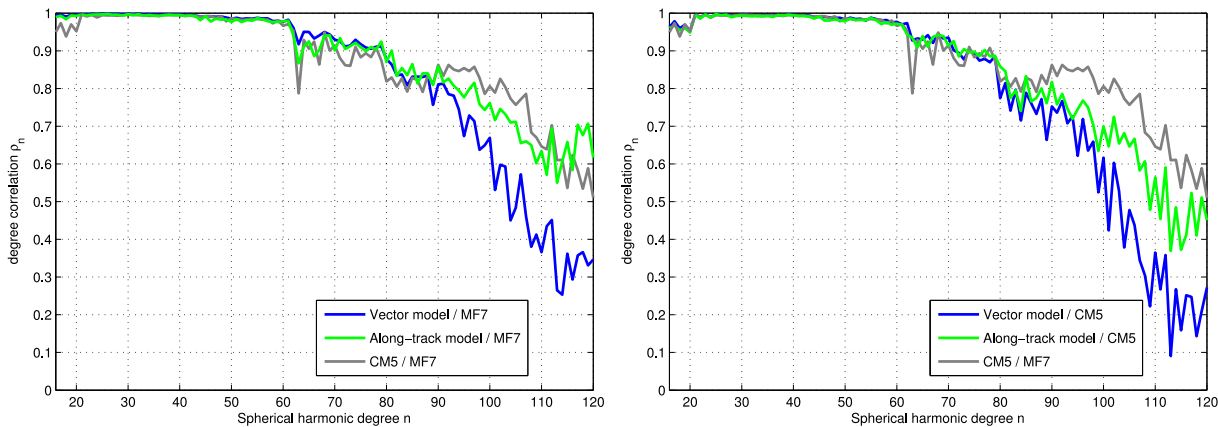

Figure 5. Degree correlation of vector (blue) and along-track (green) models with respect to MF7 (left-hand panel) resp. CM5 (right-hand panel) as well as of CM5 with respect to MF7 (grey).
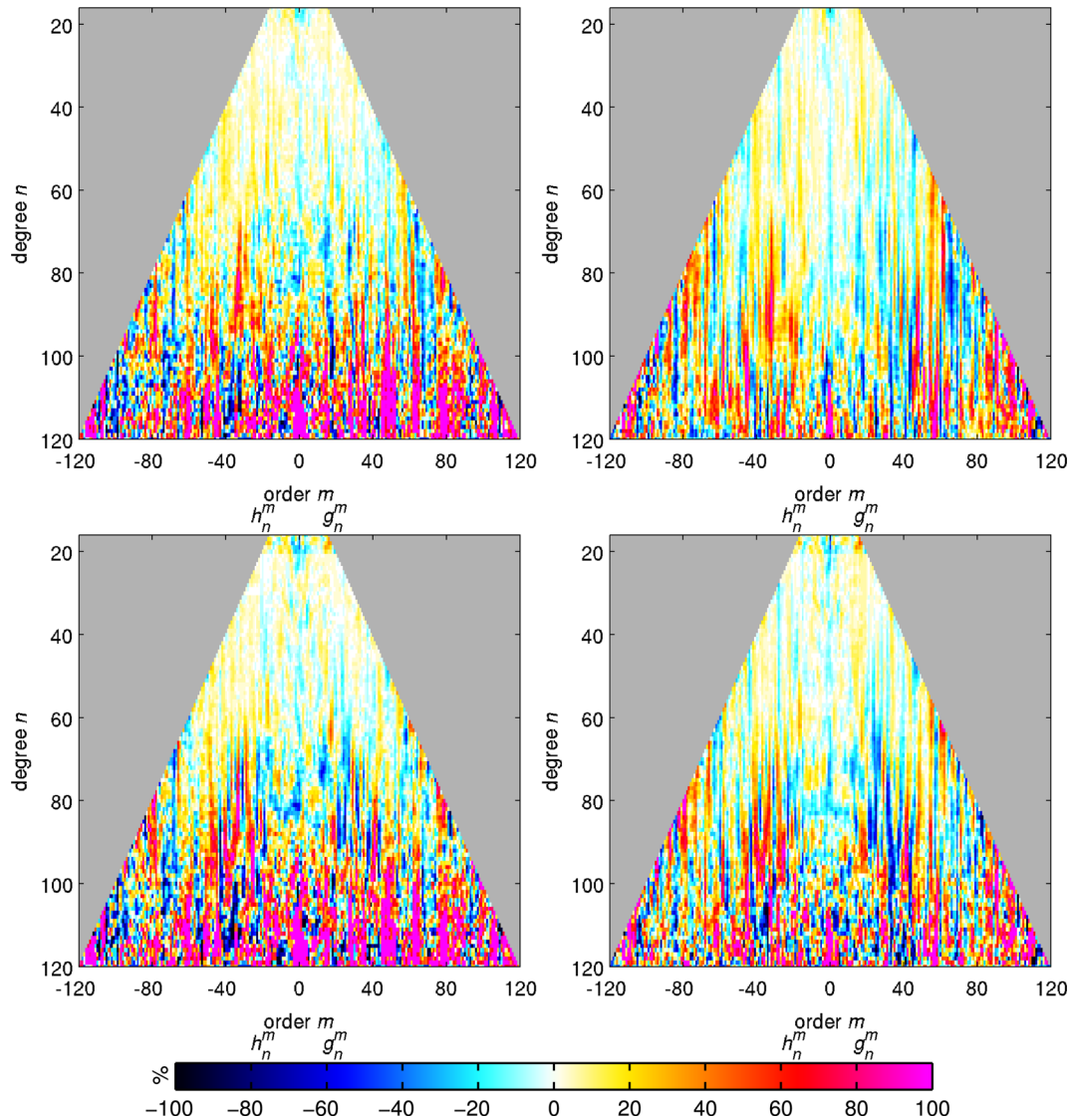
Figure 6. Sensitivity matrices (normalized coefficient differences in percent) between MF7 and the vector model (top left-hand panel), resp. along-track model (top right-hand panel) as well as between CM5 and the vector model (bottom left-hand panel), resp. along-track model (bottom right-hand panel).

determines the zonal and near-zonal coefficients than does the vector model, especially for the higher degrees. This is in accordance with fig. 4 of Kotsiaros & Olsen (2014) who pointed out that ideal north–south gradients enhance the determination of the zonal and near-zonal coefficients. We can also see that there are certain spherical harmonic orders, m, for example $45 < m < 55$, $60 < m < 70$ and $75 < m < 85$, where the differences between the vector model and both CM5 and MF7 are particularly large. These features are significantly suppressed in the along-track model.

A final comparison between our vector and along-track models and MF7 and CM5 involves the analysis of maps of the differences in their predicted radial magnetic fields at the Earth's surface, as shown in Fig. 7. These maps allow us to see where in geographical space these models differ most. The top panel shows the differences between MF7 and the vector model (left-hand part) and the along-track model (right-hand part). Similarly, the middle panel shows the differences between CM5 and the vector model (left-hand part) and the along-track model (right-hand part). For comparison, the differences between the vector and the along-track models are also shown in the bottom panel. These maps were produced using de-

grees $n = 16$–90 of the respective lithospheric field models. Both the vector and the along-track models show relatively good agreement with each other as well as with CM5 and MF7 up to degree $n = 90$. The largest differences occur in polar regions due to the unmodelled field perturbations caused, for example, by the polar electrojets. The differences in the polar regions are only slightly less for along-track model than for the vector model, indicating that along-track differences cannot solve all the problems associated with rapidly varying, small-scale perturbations in this region. We note that the differences in the polar regions between both our vector and along-track models and CM5 are larger than those with MF7. Prominent north–south oriented stripes are notable in the differences of our models with MF7, these are also seen to a lesser extent in the differences with CM5. Such features have also been documented by Olsen *et al.* (2014) in their comparison between CHAOS-4 with MF7. We can further see in our case that the north–south stripes are larger for the along-track model. Although our along-track clearly performs very well for near zonal (i.e. $n \approx 0$) coefficients, it may have deficiencies in the sectoral (i.e. $n \approx m$) coefficients (see also Fig. 6) which are known to be less well constrained by north–south
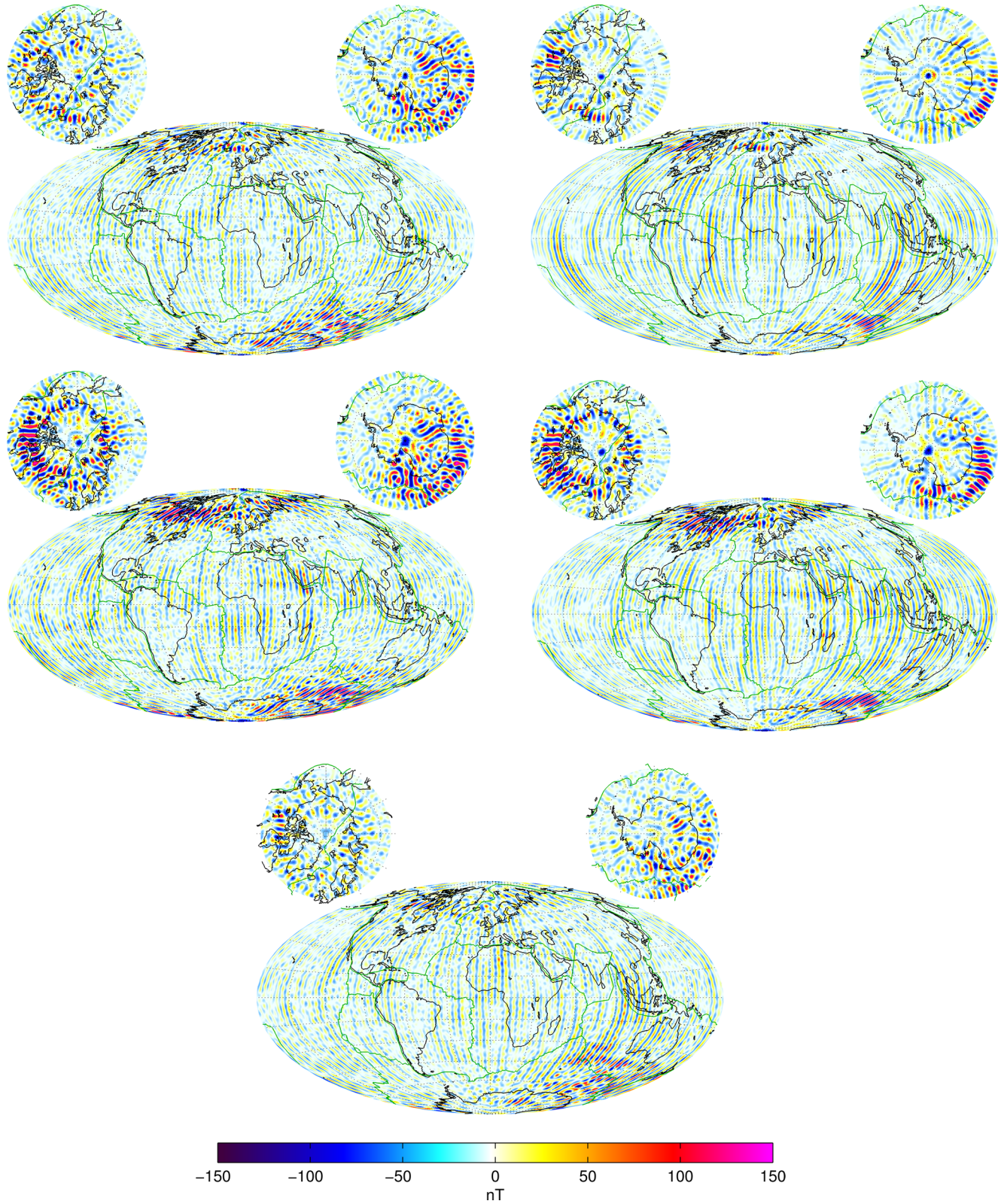
Figure 7. Maps of radial lithospheric magnetic field differences calculated at the Earth's surface from coefficients of degrees $n = 16$–90 between MF7 (top panels) resp. CM5 (middle panels) and the vector model (left-hand panels) resp. the along-track model (right-hand panels), as well as between the vector and the along-track model (bottom panel).
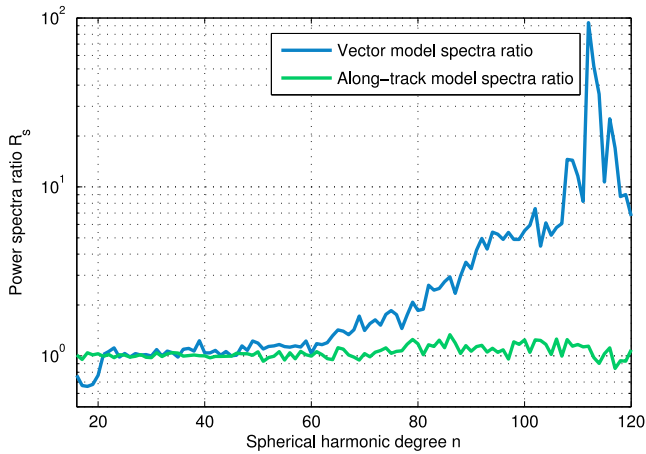
Figure 8. Ratio of spectra between the vector model (blue) resp. along-track model (green) estimated without external correction and the vector model (blue) resp. along-track model (green) estimated with external correction.

field gradients (Kotsiaros & Olsen 2014). Such deficiencies in the determination of sectoral coefficients can be avoided if one also has access to east–west field gradients as will be the case with Swarm.

One reason it is advantageous to use along-track differences rather the vector data is that taking along-track differences will remove that large-scale external field that has not changed between the two contributing sample times (30 s in our case). For example, the field produced by the ring current is to a first approximation uniform in the vicinity of the Earth, and the time between samples is short compared to the predominate timescales of ring current activity, so we might expect unmodelled ring current fluctuations to be attenuated when considering along-track differences. To investigate this issue further, we computed two lithospheric field models, with the same data sampling rate and model parametrization, but without applying the CHAOS-4 magnetospheric field corrections to

the data, that is using $\tilde{\mathbf{B}} = \mathbf{B}_{\mathrm{obs}} - \mathbf{B}_{\mathrm{core}}$ instead of eq. (2). In Fig. 8, we present the ratio of power spectra,

$$R_s = \frac{R_n^{\mathrm{noext}}}{R_n}, \qquad (11)$$

where R_n^{noext} is for a model derived using the data without external field corrections, while R_n is, as before, for a model derived from data with external field corrections applied. If an equally good model could be obtained without correction of the external field, we would expect $R_s = 1$ for all degrees. We find that using vector data, $R_s \gg 1$, especially above degree $n = 60$ indicating that the external field correction is essential. However, for the along-track data, we find $R_s \approx 1$ even at high degree. This very encouraging result highlights the benefits obtained by using along-track differences because they are relatively insensitive to unmodelled large scale external (magnetospheric) field fluctuations. Note that the gradient approach proposed here considers data only during quiet geomagnetic conditions. However, this finding may also open the possibility of internal field modelling using data during intermediate-disturbed conditions that are usually deemed unsuitable.

A final advantage of using along-track difference data regards the problem of polar gaps. Polar orbiting satellites leave non-sampled regions of half-angle $|90 - i|$ around the geographic poles, where i is the inclination of the orbit. If not dealt with, this causes a deterioration in the estimation of particularly the zonal ($m = 0$) coefficients, resulting in ringing in physical space at the geographic poles. Above, we handled this problem by adding synthetic data values of B_r within the polar gap from an *a priori* model, CHAOS-4. This technique has been used in previous high degree lithospheric field models (e.g. Maus *et al.* 2008; Lesur *et al.* 2013; Olsen *et al.* 2014). We have also derived vector and along-track models without filling the polar gap with synthetic data values. The resulting sensitivity matrices for these models with respect to MF7 are shown in Fig. 9 with the vector model shown in the left-hand panel and along-track model in the right-hand panel. As expected, in the vector model the zonal coefficients are poorly determined with large differences compared to MF7 starting already from degree 20. Due to
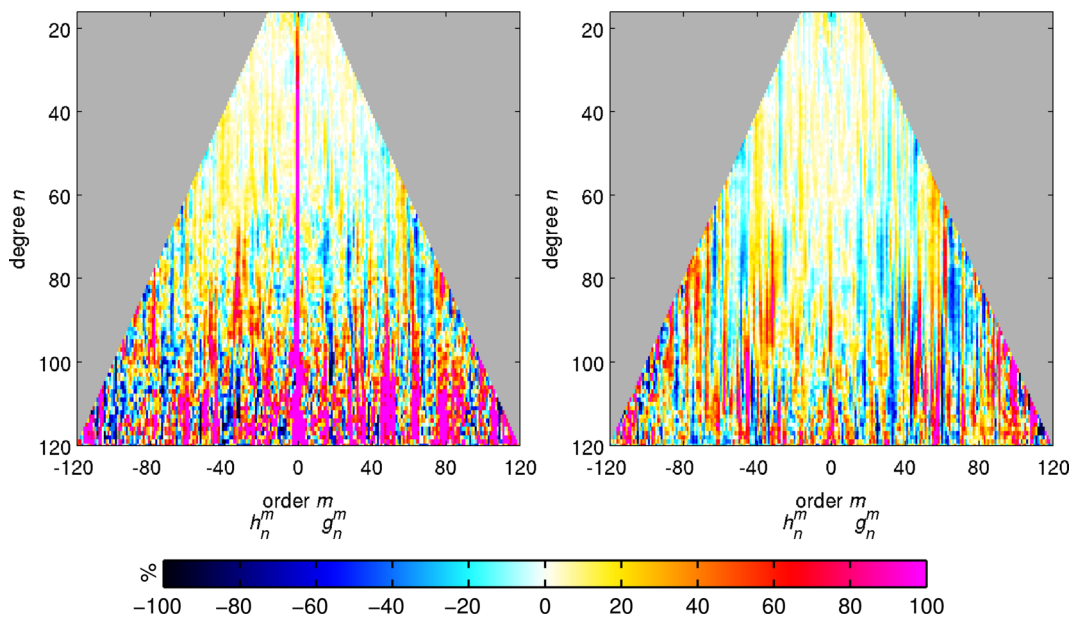
Figure 9. Sensitivity matrices (normalized coefficient differences in percent) between MF7 and the vector model (left-hand panel), resp. along-track model (right-hand panel) without filling the polar gap with synthetic data values of B_r.

the inclined satellite orbit, along-track differences in polar regions approximate a mixture of north–south with a substantial contribution of east–west gradients which are sensitive to sectoral ($n = m$) and tesseral ($m \neq 0$ and $m \neq n$) coefficients (rather than to zonal and near-zonal coefficients). Therefore, similarly to the vector model, deficiencies in the zonal coefficients associated with the polar gap could conceivably also appear in the along-track model. However, in fact we find the problem is much less severe in the along-track model, where obvious deficiencies appear first above degree 80. An explanation for the improved tolerance of along-track difference data to the polar gap is provided by considering the Green's function for the Neumann boundary value problem. Specifically,

$$B_j(\mathbf{r}) = \int_{S'} G_j(\mathbf{r}, \mathbf{r}') B_r(\mathbf{r}') \, dS', \qquad (j = r, \theta, \phi) \tag{12}$$

describes how a vector field observation B_j at location $\mathbf{r}$ can be represented as a weighted integral of the radial field B_r at an internal reference surface S'. The weights are provided by Green's functions G_j that describe the effective sensitivity of the observation to the field on the reference surface. Following Gubbins & Roberts (1983), the Green's functions

$$G_r = \frac{b^2}{4\pi} \frac{(1 - b^2)}{f^3}, \tag{13}$$

$$G_h = \frac{b}{4\pi} \left[\frac{1 - 2b\mu + 3b^2}{f^3} + \frac{\mu}{f(f + b - \mu)} - \frac{1}{1 - \mu} \right]$$
$$\times (1 - \mu^2)^{1/2} \tag{14}$$

describe how measurements of the vertical, B_r, resp. horizontal, B_θ and B_ϕ, field components of an observation at $r = r_0$ (e.g. at satellite altitude) depend on the radial field at the Earth's surface. Above, we have used $b = a/r_0$, $f = (1 - 2\mu b - b^2)^{1/2}$, whereas with α the angle between the point of observation, (θ, ϕ), and the point under consideration on the Earth's surface, (θ', ϕ'), and $\mu = \cos\alpha = \sin\theta\sin\theta'\cos(\phi - \phi') + \cos\theta\cos\theta'$. To obtain G_h, without the loss of generality, the observation site was placed at $\theta = 0, \phi = 0$ which results in $\mu = \cos\theta'$.

Similar Green's functions for the horizontal gradients of the vertical component B_r are obtained as follows:

$$G_{r\theta} = \left(\frac{1}{r} \frac{\partial G_r}{\partial \theta} \right)_{r=r_0} = \left(\frac{1}{r} \frac{\partial G_r}{\partial \mu} \right)_{r=r_0} \frac{\partial \mu}{\partial \theta}, \tag{15}$$

$$G_{r\phi} = \left(\frac{1}{r \sin\theta} \frac{\partial G_r}{\partial \phi} \right)_{r=r_0} = \left(\frac{1}{r} \frac{\partial G_r}{\partial \mu} \right)_{r=r_0} \frac{1}{\sin\theta} \frac{\partial \mu}{\partial \phi}. \tag{16}$$

Again, without loss of generality, we can place the observation site at $\theta = 0, \phi = 0$ which leads to

$$G_{r\theta} = \partial_h G_r \cos\phi', \tag{17}$$

$$G_{r\phi} = \partial_h G_r \sin\phi'. \tag{18}$$

with

$$\partial_h G_r = \left(\frac{1}{r} \frac{\partial G_r}{\partial \mu} \right)_{r=r_0} = \frac{3b^3(1 - b^2)}{4\pi r_0 f^5} (1 - \mu^2)^{1/2}. \tag{19}$$

Fig. 10 presents the functions G_r and G_h for the vertical and horizontal components respectively, as well as the function $\partial_h G_r$ relevant for horizontal gradients of the vertical component, plotted at $r_0 = a + 400$ km as a function of the angular distance θ' away from the observation point. $\theta' = 0$ here corresponds to the point on the Earth's surface immediately beneath the observation site. The
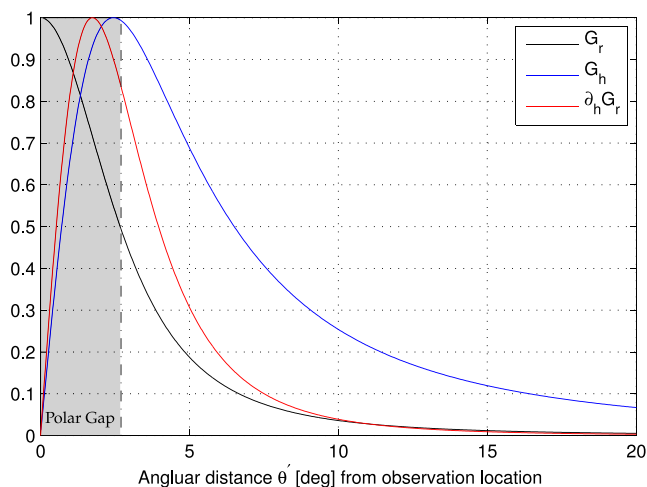

Figure 10. Normalized Green's functions G_r and G_h for the vertical and horizontal field components, respectively, as well as the function $\partial_h G_r$ relevant for horizontal gradients of the vertical component for $r_0 = a + 400$ km as a function of the angular distance θ' from the observation location. $\theta' = 0$ corresponds to the point on the Earth's surface immediately beneath the observation site.

polar gap region for CHAMP is indicated in grey. For example, if an observation was at the highest latitude for CHAMP (i.e. 87.3°), then $\theta' = 2.7°$ in this plot would correspond to the North Pole. For plotting purposes, the Green's functions have been normalized with respect to their maximum amplitude to 1. Fig. 10 illustrates the sensitivity of different types of observations at satellite altitude to the internal source field, on Earth's surface. In particular, the radial vector field measurements are primarily sensitive to the field directly beneath the measurement site, which leads to a polar gap problem when they are used alone. The horizontal components B_θ, B_ϕ and the horizontal gradients of B_r however predominantly sample the field at an angular distance away from the observation site (approximately 2.5° and 1.8°, respectively). Using measurements of B_θ and B_ϕ would therefore ameliorate the polar gap problem, but unfortunately these components are disturbed by high-latitude ionospheric currents and they are consequently not normally used in polar regions. On the other hand, we have shown above that horizontal gradients of B_r are less affected by such currents and Fig. 10 illustrated that they also tolerate gaps in the orbit tracks including the polar gap.

5 CONCLUSIONS AND OUTLOOK

We have constructed high resolution lithospheric field models using first differences of CHAMP vector field data along each satellite orbit track. Compared to a model derived from the same data set and using the same model parametrization, but constructed only using vector field data, we find that the along-track model better reconstructs both the amplitude and the phase of the high degree field. Near-zonal spherical harmonic coefficients were especially well recovered. Furthermore, in order to derive a precise high-degree lithospheric field model using along-track differences, a correction or an explicit co-estimation of the magnetospheric field contribution is not so critical as is the case when using vector field data. This is due to along-track differences being less sensitive to large-scale external field fluctuations varying on time scales longer than the sampling rate.

The proof of concept presented in this work involved deriving non-regularized lithospheric field models with a focus on investigating the possible benefits of using along-track differences rather than aiming to derive superior models to the existing ones. In addition to the relatively simple field modelling experiments reported here, along-track differences have also now been used in sophisticated, state-of-the-art field modelling scheme involving full co-estimation of sources (Sabaka *et al.* 2014). The findings of Sabaka *et al.* (2014) provide further support for the conclusions reached above concerning the advantages of using along-track data to determine the high degree lithospheric field. Given that the required modifications to existing modelling schemes are minor, the case for using along-track differences, especially in combination with east–west field differences, is compelling.

The recently launched Swarm mission will allow a unique space–time characterization of both sources within the Earth and also the ionospheric–magnetospheric current systems. It consists of two low-altitude satellites, which allow cross-track magnetic gradients to be estimated, and a third satellite at higher altitude which monitors the field at different local times. The data products of the Swarm mission are described by Olsen *et al.* (2013). As an extension of the work presented here, we plan to use Swarm data to derive estimates of east–west gradients and combine them with north–south gradients approximated by along-track differences. These two gradients carry complementary information, for example see fig. 2 of Kotsiaros & Olsen (2012), and their combination holds great promise for an improved determination of not only the lithospheric field but also the high degree secular variation.

REFERENCES

Backus, G., Parker, R. & Constable, C., 1996. *Foundations of Geomagnetism,* Cambridge Univ. Press.

Connerney, J.E.P., Acua, M.H. Ness, N.F., Kletetschka, G., Mitchell, D.L., Lin, R.P. & Reme, H., 2005. Tectonic implications of Mars crustal magnetism, *Proc. Natl. Acad. Sci. U.S.A.*, **102**(42), 14 970–14 975.

Constable, C.G., 1988. Parameter estimation in non-Gaussian noise, *Geophys. J.,* **94,** 131–142.

Friis-Christensen, E., Lühr, H. & and Hulot, G., 2006. Swarm: a constellation to study the Earth's magnetic field, *Earth Planets Space,* **58**(4), 351–358.

Gubbins, D. & Roberts, N., 1983. Use of the frozen flux approximation in the interpretation of archaeomagnetic and palaeomagnetic data, *Geophys. J. R. astr. Soc.,* **73,** 675–687.

Huber, P.J., 1964. Robust estimation of a location parameter, *Ann. Math. Stat.*, **35**(1), 73–101.

Kotsiaros, S. & Olsen, N., 2012. The geomagnetic field gradient tensor, *GEM Int. J. Geomath.,* **3,** 297–314.

Kotsiaros, S. & Olsen, N., 2014. End-to-end simulation study of a full magnetic gradiometry mission, *Geophys. J. Int.,* **196**(1), 100–110.

Kunagu, P., Balasis, G., Lesur, V., Chandrasekhar, E. & Papadimitriou, C., 2013. Wavelet characterization of external magnetic sources as observed by CHAMP satellite: evidence for unmodelled signals in geomagnetic field models, *Geophys. J. Int.,* **192**(3), 946–950.

Langel, R.A. & Hinze, W., 1998. *The Magnetic Field of the Earth's Lithosphere: The Satellite Perspective,* pp. 113–122, Cambridge Univ. Press.

Lesur, V., Rother, M., Vervelidou, F., Hamoudi, M. & Thébault, E., 2013. Post-processing scheme for modelling the lithospheric magnetic field, *Solid Earth,* **4**(1), 105–118.

Lowes, F.J., 1974. Spatial power spectrum of the main geomagnetic field, and extrapolation to the core, *Geophys. J. R. astr. Soc.,* **36,** 717–730.

Lühr, H., Rother, M., Maus, S., Mai, W. & Cooke, D., 2003. The diamagnetic effect of the equatorial Appleton anomaly: its characteristics and impact on geomagnetic field modeling, *Geophys. Res. Lett.,* **30**(17), 1906, doi:10.1029/2003GL017407.

Maus, S. *et al.*, 2008. Resolution of direction of oceanic magnetic lineations by the sixth-generation lithospheric magnetic field model from CHAMP satellite magnetic measurements, *Geochem. Geophys. Geosyst.,* **9**(7), Q07021, doi:10.1029/2008GC001949.

Olsen, N., 2002. A model of the geomagnetic field and its secular variation for epoch 2000 estimated from Ørsted data, *Geophys. J. Int.,* **149**(2), 454–462.

Olsen, N. & Stolle, C., 2012. Satellite geomagnetism, *Ann. Rev. Earth planet. Sci.,* **40**(1), 441–465.

Olsen, N., Lühr, H., Sabaka, T.J., Mandea, M., Rother, M., Tøffner-Clausen, L. & Choi, S., 2006. CHAOS—a model of the Earth's magnetic field derived from CHAMP, Ørsted, and SAC-C magnetic satellite data, *Geophys. J. Int.,* **166**(1), 67–75.

Olsen, N., Lühr, H., Finlay, C.C., Sabaka, T.J., Michaelis, I., Rauberg, J. & and Tøffner-Clausen, L., 2014. The CHAOS-4 geomagnetic field model, *Geophys. J. Int.,* **197**(2), 815–827.

Olsen, N. *et al.*, 2013. The Swarm Satellite Constellation Application and Research Facility (SCARF) and Swarm data products, *Earth Planets Space,* **65**(11), 1189–1200.

Reigber, C., Lühr, H., Schwintzer, P. & Wickert, J., 2005. *Earth Observation with CHAMP: Results from Three Years in Orbit,* Springer-Verlag.

Richmond, A.D., 1995. Ionospheric electrodynamics using magnetic apex coordinates, *J. Geomagn. Geoelectr.,* **47,** 191–212.

Sabaka, T., Tøffner-Clausen, L. & Olsen, N., 2013. Use of the comprehensive inversion method for Swarm satellite data analysis, *Earth Planets Space,* **65**(11), 1201–1222.

Sabaka, T.J., Olsen, N., Tyler, R.H. & Kuvshinov, A., 2014. CM5, a pre-Swarm comprehensive geomagnetic field model derived from over 12 years of CHAMP, Ørsted, SAC-C and observatory data, *Geophys. J. Int.,* in press.

Thébault, E., Purucker, M., Whaler, K.A., Langlais, B. & Sabaka, T.J., 2010. The magnetic field of the Earth's lithosphere, *Space Sci. Rev.,* **155,** 95–127.

Thébault, E., Vigneron, P., Maus, S., Chulliat, A., Sirol, O. & Hulot, G., 2013. Swarm SCARF Dedicated lithospheric field inversion chain, *Earth Planets Space,* **65**(11), 1257–1270.

Walker, M.R. & Jackson, A., 2000. Robust modelling of the Earth's magnetic field, *Geophys. J. Int.,* **143,** 799–808.